Research
Hydraulic Engineering—Article

# Recognition of Fluvial Bank Erosion Along the Main Stream of the Yangtze River

Ge Yan [a], Heqin Cheng [a,c,*], Zeyu Jiang [a], Lizhi Teng [a], Ming Tang [a], Tian Shi [a], Yuehua Jiang [b], Guoqiang Yang [b], Quanping Zhou [b]

[a] State Key Laboratory of Estuarine and Coastal Research, East China Normal University, Shanghai 200000, China
[b] Nanjing Center, China Geological Survey, Nanjing 210000, China
[c] Institute of Eco-Chongming, Shanghai 200000, China

## ARTICLE INFO

## ABSTRACT

Recognizing the risk of fluvial bank erosion is an important challenge to ensure the early warning and prevention or control of bank collapse in river catchments, including in the Yangtze River. This study introduces a geomorphons-based algorithm to extract river bank erosion information by adjusting the flatness from multibeam echo-sounding data. The algorithm maps ten subaqueous morphological elements, including the slope, footslope, flat, ridge, peak, valley, pit, spur, hollow, and shoulder. Twenty-one flatness values were used to build an interpretation strategy for the subaqueous features of riverbank erosion. The results show that the bank scarp, which is the erosion carrier, is covered by slope cells when the flatness is 10°. The scour pits and bank scars are indicated by pit cells near the bank and hollow cells in the bank slope at a flatness of 0°. Fluvial subaqueous dunes are considered an important factor accelerating bank erosion, particularly those near the bank toe; the critical flatness of the dunes was evaluated as 3°. The distribution of subaqueous morphological elements was analyzed and used to map the bank erosion inventory. The analysis results revealed that the near-bank zone, with a relatively large water depth, is prone to form large scour pits and a long bank scarp. Arc collapse tends to occur at the long bank scarp to shorten its length. The varied assignment of flatness values among terrestrial, marine, and fluvial environments is discussed, concluding that diversified flatness values significantly enable fluvial subaqueous morphology recognition. Consequently, this study provides a reference for the flatness-based recognition of fluvial morphological elements and enhances the targeting of subaqueous signs and risks of bank failure with a range of multibeam bathymetric data.

## 1. Introduction

Bank erosion is a severe problem in any fluvial system, as it can contribute to a majority of the total sediment load in a catchment [1–3]. It causes damage to structures and land loss adjacent to the river channel, leading to various alterations to the riverbed and floodplain [4,5]. Since the closure of the Three Gorges Dam, the bank slope has been frequently unstable during intensified erosion of the main stream in the middle and lower reaches of the Yangtze River. Bank erosion in an alluvial river downstream of a dam is important for flood control management, and this topic has

received significant attention recently [6,7]. Evaluations of the erosion rate using observation records of multi-periods have been conducted for decades [8–10]. Many studies have focused on modeling bank erosion using geographic information system (GIS)-based vulnerability zonation technology [11,12], as well as combining bank stability with fluvial processes, such as toe erosion [13] and bed deformation [14]. Recently, novel measurement instruments have been applied to analyze the mechanism of bank erosion, including terrestrial laser scanners, acoustic Doppler current profilers, and multibeam echo-sounding systems [15]. Motion photogrammetry, along with high-resolution topographic data, have been used to monitor the erosion of terrestrial banks [16]. However, most bank erosion occurs under water in the main channel of the middle and lower reaches of the Yangtze River, where most parts of the bank slope are submerged by water.

---

Identification of subaqueous bank erosion has become essential for raising early alarms, thereby being an important and urgent issue for decision makers and planners.

Measurement records from multibeam eco-sounding systems provide a method to create high-resolution bathymetric data that are used to generate slope [17,18] or shade relief maps [19,20]. Subaqueous morphological element maps are also in demand to gain additional knowledge on bank erosion. To map morphological elements, Wood [21] divided the land surface into six elements, including the channel, ridge, plane, peak, pit, and pass, based on the slope and curvature. Macmillan et al. [22] applied heuristic rules and fuzzy logic to combine topographic variables, such as relatively convex, concave, and planar in profile, to classify 15 elements, including level crest, divergent shoulder, upper depression, and back-slope. The advancement of computing technology has led to the development of an increasing number of methods. The iterative self-organizing data analysis technique has been used to extract ten elements from a digital elevation model (DEM) [23]. A top-hat method was combined with Wood's method to generate nine elements, including ridge, shoulder, and back-slope, from the DEM using threshold values of the slope, curvature, and elevation [24]. An object-based image analysis method was applied to segment nine elements from four parameters, including elevation, profile curvature, plan curvature, and slope gradient [25]. A pattern recognition approach (geomorphons) was used to extract elements on the terrestrial surface from elevation based on local ternary patterns (LTPs) and the line-of-sight principle [26]. Geomorphons were also used in the sea environment by Cui et al. [27] to classify morphological elements of the sea floor at relatively large cell sizes. In addition, the method of geomorphons was found to be superior to Wood's criteria for describing submarine dunes [28]. A different method based on geodesic morphometry was also applied to automatically extract dune crests and troughs [29].

In a river system, algorithmic techniques can be efficient for auto-extraction of morphological elements. This study applies geomorphons to recognize subaqueous features of bank erosion, including the bank scarp, bank scar, and scour pit, as well as the bank toe and dunes. A bank scarp that hosts a steep slope is the carrier of bank erosion. Bank scars and scour pits are considered the vestiges of bank erosion. The bank toe retreats during bank erosion and affects bank stability. The movement of dunes changes the bed forms that influence the flow-field environment and then partially affects the process of bank erosion, specifically when the dune is developed near the bank. We applied the method of geomorphons owing to its flexibility in various regions [26,27,30–35]. Our study can be differentiated from many existing studies because it analyzes the significance of setting a suitable flatness for morphological element mapping.

## 2. Study area

The study reach of the Yangtze River is just upstream from the confluence of the Yangtze River and Dongting Lake, situated approximately 390 km downstream from the Three Gorges Dam. The reach is in an S-shape with a length of 25 km and within the longitudes and latitudes of 113°4′E–113°8′E and 29°26′N–29°30′ N, respectively. The study reach borders the Hubei Province and Hunan Province in the north and south, respectively. Fig. 1(a) displays the vectors of the water depths, shallow areas (the area above a water depth of 0 m), and riverbank generated from a navigation map of the middle reaches of the Yangtze River in 2015, with digital processing based on the navigation datum of the Yangtze River in 1958 and the national elevation datum in 1985. The reach can be divided into channels from Qizhou to

Chenglingji, from Linjiaolao to Qizhou, and upstream of Linjiaolao. The riverbed is covered by sand within the shallow area, which is exposed above the water surface in the dry season.

Bank erosion is severe in this reach; based on a 2019 survey, almost all the banks along the main channel are occupied by failures. Bank failure was classified as wash collapse, strip collapse, and arc collapse [36,37]. Our field investigation showed that strip and arc collapses along the riverbank are the most prevalent failure modes in the reach. The bank slope still faces a severe risk of failure despite bank protection measures (Fig. S1 in Appendix A). For the natural fluvial bank, the upper stratum, consisting of cohesive soil with a high degree of consolidation, and the loose sand stratum at the foot of the slope often lead to strip collapse after the bank carves and loses support [38]. Arc collapse is highly destructive and usually occurs at the top of a concave bank with a relatively large scour depth and curvature [39]. Bank failure affects the evolution of the river course and changes the river regime. During the evolution of the river course, the swing of the main stream line and erosion of the river course may cause bank failure. If bank failure along the river course is not controlled promptly, it may lead to adjustments to the river regime [40].

## 3. Methodology

### 3.1. Data acquisition

Field measurements were conducted from August 27–29, 2019. Bathymetric data were acquired at a water depth of 1–45 m using a Reson SeaBat T50-P multibeam system operating at frequencies of 200/400 kHz. Data were Differential Global Positioning System (DGPS)-positioned and processed with the Teledyne PDS software package, USA. To ensure data collection of the water depth, the ship speed was controlled within eight knots. Universal Transverse Mercator (UTM) 50 N was selected as the projection reference system. The multibeam echo-sounding system scanned a total length of 72.32 km, mainly the left bank adjacent zone upstream of Linjiaolao, the right bank adjacent zone from Linjiaolao to Qizhou, and the main channel from Qizhou to Chenglingji.

Then, we manually removed the outliers from the point cloud of the water depth using the editing tool in the latest version of the PDS software. Numerous notable outliers can be selected and deleted. The processed point cloud was used to generate a grid model with a grid spacing of 0.5 m, resulting in a total of approximately 15.37 million grids for the entire area. The grid model was imported into the ArcGIS version 10.3 software package, as shown in Fig. 1(a), and used as the input for the geomorphons method to map the subaqueous morphological elements for bank erosion recognition. Six sample areas were selected and named "near-bank zone" (NBZ), represented as NBZs 1–6 for the following analyses (Fig. 1(b)).

### 3.2. Principle of geomorphons and subaqueous morphological elements

In the geomorphons method, the LTP method developed by Liao [41], describes the terrain types in the vicinity of the central cell. The terrain was used as input to identify ten surface morphological elements based on the local elevation of terrain (Fig. 2(a) [26]). The morphological elements can be regrouped into three classes, including convex elements (ridge, shoulder, peak, and spur), straight elements (slope and flat), and concave elements (valley, footslope, pit, and hollow).

Practically, an LTP was determined from a combination of eight elevation changing trends, starting at the central cell and extending along the principal compass directions (D) up to the lookup
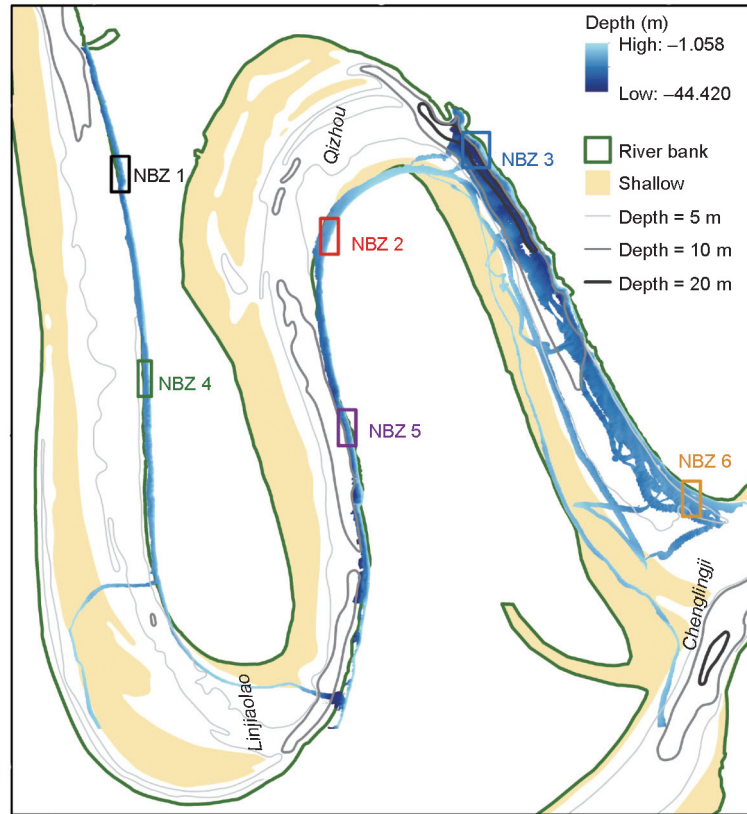
(a)
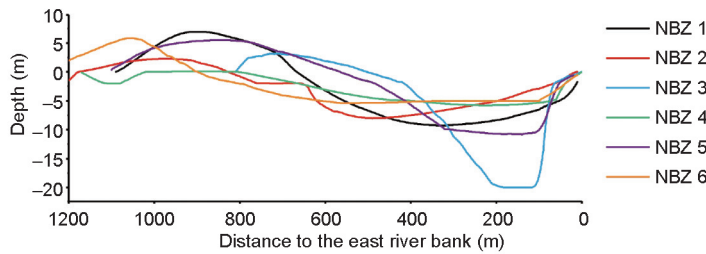


(b)

**Fig. 1.** (a) Measured multibeam bathymetric data and (b) the transect profile of the sample area.

distance ($L$), extracted using the line-of-sight principle [42]. The eight elevation profiles were extracted from the DEM to calculate the zenith ($\phi_L^D$) and nadir angles ($\psi_L^D$) at the central cell. The zenith and nadir angles were used to indicate the openness of the terrain surface and were calculated based on the elevation angle of the profile. There are eight principal compass directions for each central cell, that is, north (N), south (S), west (W), east (E), northeast (NE), southwest (SW), northwest (NW), and southwest (SE), at intervals of 45°. Along each direction, a set of elevation angles were calculated from the profile. An elevation angle is defined as the angle between the horizontal plane and a line connecting the central cell to a point located on the profile. Negative and positive elevation angles are associated with points on the profile lower and higher than the central cell, respectively. Within the lookup distance ($L$) in direction ($D$), the zenith and nadir angles along the lookup distance and direction can be calculated from the maximum elevation angle ($\beta_L^D$) and minimum elevation angle ($\delta_L^D$) as follows:

$$\begin{aligned} \phi_L^D &= 90° - \beta_L^D \\ \psi_L^D &= 90° + \delta_L^D \end{aligned} \tag{1}$$

Fig. 2(b) [26] illustrates the concept of the zenith ($\phi$) and nadir ($\psi$) angles. For point A, both the maximum and minimum elevation angle are negative, yielding a zenith angle greater than 90° and nadir angle smaller than 90°. Therefore, the zenith and nadir angles both vary in the range of 0°–180°. The elevation changing trend of a profile corresponding to direction ($D$) and lookup distance ($L$) is represented by the difference between the zenith and nadir angles. Flatness ($t$), also known as the relief threshold, is a minimum value of the difference between the zenith and nadir angles considered significantly different from the horizon. This was used to divide the difference into three classes denoted by $\Delta_L^D$ as follows:

$$\Delta_L^D = \begin{cases} 1 & \text{if} \quad \phi_L^D - \psi_L^D < -t \\ 0 & \text{if} \quad |\phi_L^D - \psi_L^D| \le t \\ -1 & \text{if} \quad \phi_L^D - \psi_L^D > t \end{cases} \tag{2}$$
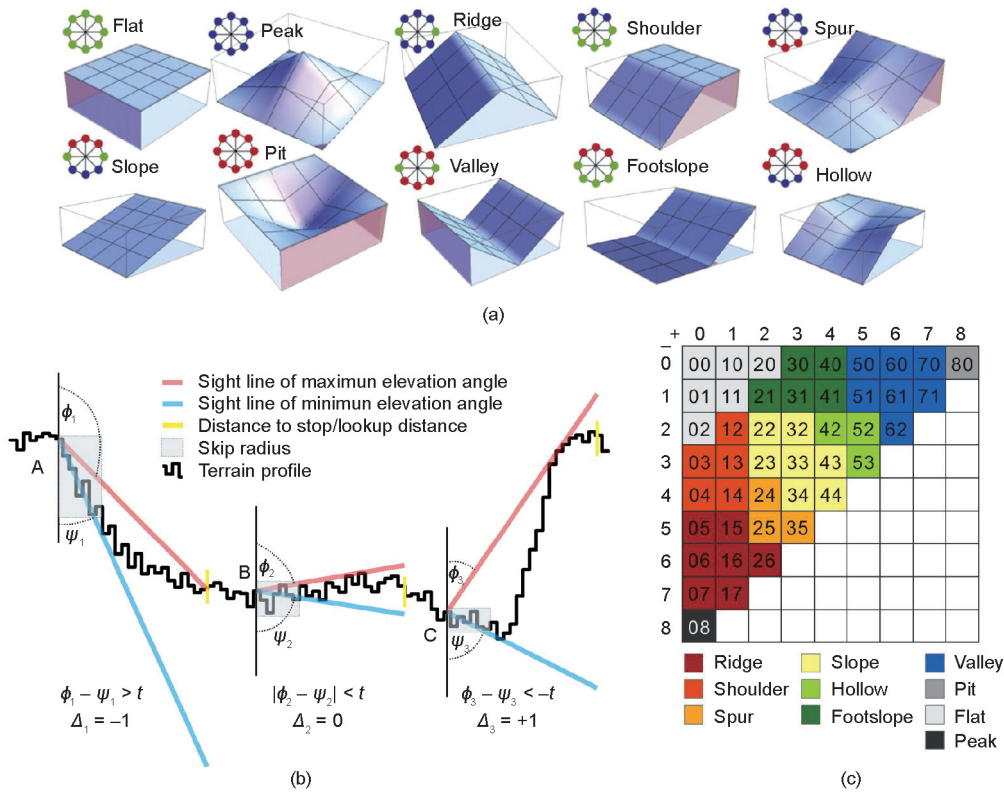
**Fig. 2.** (a) Illustrations of the LTPs, (b) line-of-sight principle, and (c) lookup table in the geomorphons-based auto-classification of morphological elements. A, B, and C in (b) are three central cells as the cases to show three typical assignments of $\Delta$ based on the comparison among the zenith ($\phi$) and nadir angles ($\psi$), and flatness ($t$). In (c) the elements are defined based on the number of ($-1$) and ($+1$) symbols that combined into a two-digit number. Reproduced from Ref. [26] with permission.

where (0), ($-1$), and ($+1$) represent that the surface profile from the central cell is horizontal, downward, and upward, respectively. The three typical effects corresponding to the symbol are shown in Fig. 2(b) [26], where $\Delta_L^D$ is represented as $\Delta$. Moreover, eight symbols for a ternary pattern were calculated as each elevation profile has one $\Delta_L^D$.

With three possible values for $\Delta_L^D$ in each of the eight directions, the total number of possible LTPs is $3^8$ (i.e., 6561). Only 498 different LTPs remain after considering rotational and reflectional symmetries, which are defined as geomorphons [26]. Jasiewicz and Stepinski [26] established a lookup table for terrestrial landform elements (Fig. 2(c)), where the rows and columns indicate the number of ($-1$) and ($+1$) symbols in the pattern, respectively. Using the lookup table, ten morphological elements were defined by grouping geomorphons based on the number of ($-1$) and ($+1$) symbols, which were considered as the ten subaqueous morphological elements.

### 3.3. Presupposition of lookup distance, skip radius, and flatness

The parameters used to effectively apply the geomorphons method for subaqueous bank erosion recognition are the lookup distance ($L$) and flatness ($t$), as indicated in Eq. (2), and the skip radius, as presented in Fig. 2(b) [26]. Here, $L$ determines the size of the traversal window. This window should be relatively large to contain the bank scarp, whereas a small window is sufficient to include bank scars and scour pits. When the window size is larger than a certain threshold, the mapping result is constant because zenith and nadirs angles will change little with further increase of window size. Using a greater lookup distance, we can simultaneously identify elements on a wider range of scales. For example, Jasiewicz and Stepinski [26] considered 50 cells as the critical lookup distance. Accordingly, we set the lookup distance

as 100 m, which is sufficient to cover the data for the water depth from the bank slope to the riverbed. A larger window size was not considered because the large lookup distance increases the computational pressure and has little contribution to element mapping.

The skip radius is used to filter the influence of small terrain changes in the vicinity of the central cell (Fig. 2(b) [26]). As mentioned above, removing the outliers that are not notable in the editing tool is difficult, and the outliers near the central cell interfere with the identification of morphologic elements. Therefore, by setting the skip radius such that the terrain change near the central cell is neglected, the calculation began at values greater than the skip radius. In this study, the skip radius was 3 m, that is, the water depth variation in the distance within six cells near the central cell for the N, E, S, and W directions, and within four cells for the NW, NE, SW, and SE directions.

The flatness value varies from 1° to 3° in different studies [26,27,31–35]. Theoretically, with a decrease in the flatness, the number of ($-1$) and ($+1$) symbols can both increase, indicating that more subaqueous surfaces originally covered by flat cells can be classified into other elements. Adjusting the flatness value to generate and compare the morphological element maps is necessary. Then, a suitable flatness value for the classification of underwater surfaces and the recognition of bank erosion features can be determined. Twenty-one flatness values were selected to generate morphological element maps to show the trend of decreasing flatness: 40°, 35°, 30°, 25°, 20°, and 15° (at intervals of 5°) and 14°, 13°, 12°, 11°, 10°, 9°, 8°,7°, 6°, 5°, 4°, 3°, 2°, 1°, and 0° (at intervals of 1°).

### 3.4. Processing procedure for morphological element mapping

The GRASS GIS software provides a tool to generate morphologic element maps. In this tool, flatness cannot be set as zero

because $|\phi_L^D - \psi_L^D| < t$ is the condition to assign 0 to $\varDelta_L^D$. In addition, it may be time consuming to map elements for various flatness values as required in this study. We scripted geomorphons in MATLAB 2019b.

To enhance the computation of the zenith and nadir angles, eight convolutions for the principal compass directions were used to move the matrix of the bathymetric data by one cell at every time instant for each direction (Fig. 3). The differences in the distance of the moving image in the N, E, S, and W directions was one grid size, whereas that in the NE, SE, NW, and NW directions was $\sqrt{2}$ times the grid size. We saved the number of (+1) and (−1) symbols as the number of tens and bits, respectively. Consequently, all the geomorphons can be represented as a two-digit number (Fig. 2(c) [26]), where, for example, 52 represents five (+1) and two (−1).

Using a computing platform with an i5 3570 central processing unit (CPU) and 16 GB memory, approximately 2.5 h was consumed without parallel computing to calculate the zenith and nadir angles in the 15 396 × 15 237 matrix for a lookup distance of 100 m. Geomorphons-based morphological elements classification through the comparison of the zenith and nadir angles required approximately 1 h for computation. The total computation time of approximately 5 h to identify the geomorphic elements of the entire study area is advantageous.

## 4. Results

### 4.1. Implication of flatness on the recognition of subaqueous morphological elements

We can map the subaqueous elements of morphology with different reliefs using various flatness values. Fig. 4 shows NBZs

4 and 6, which were used to demonstrate the distribution change in the morphological elements with the set of flatness values. There is an upward trend in the number of slope cells, but a contrasting trend for flat cells with a decrease in flatness from 40° to 3°. With a flatness of 40°, the most subaqueous area near the bank was classified as a flat element. With a flatness of 10°, the underwater bank slope was covered by slope cells. With a flatness of < 10°, the riverbed was gradually overlapped by slope, ridge, and valley cells with a further decline in the flatness. With a flatness of ≤ 3°, the pattern of elements remained steady, although the peak and pit cells expanded in the center of the ridge and valley areas.

Fig. 5 presents the statistical results of the morphological elements, and Table 1 quantitatively lists the recognition results of the geomorphons method for the morphological elements under different flatness values. With a flatness of 40°, the subaqueous surface was occupied by flat cells, accounting for approximately 95% of the area. With a flatness of 10°, the percentage of footslope cells was relatively large, approximately 9.68%–20.07%. For flatness ranging from 10° to 3°, the occupation of the slope cell increased and reached its highest point at approximately 3°. However, the percentage of flat cells sharply decreased and disappeared at 3°. This revealed that a relatively flat surface becomes a slope when the flatness value is minimal. Hollow and spur cells increased with the decrement in the flatness and reached a peak at 0°, encompassing 11.17%–20.63%. Pit cells also increased to the highest occupation of approximately 4.26%–10.33% for NBZs 1–6 with a flatness of 0°. In contrast, shoulder and footslope cells disappeared with a flatness of 0°. This can be explained by Eq. (2), where $\varDelta_L^D$ cannot be defined as (0) for $t$ = 0° and the total number of (+1) and (−1) symbols is eight, leading to the disappearance of the flat, shoulder, and footslope according to Fig. 2(c).
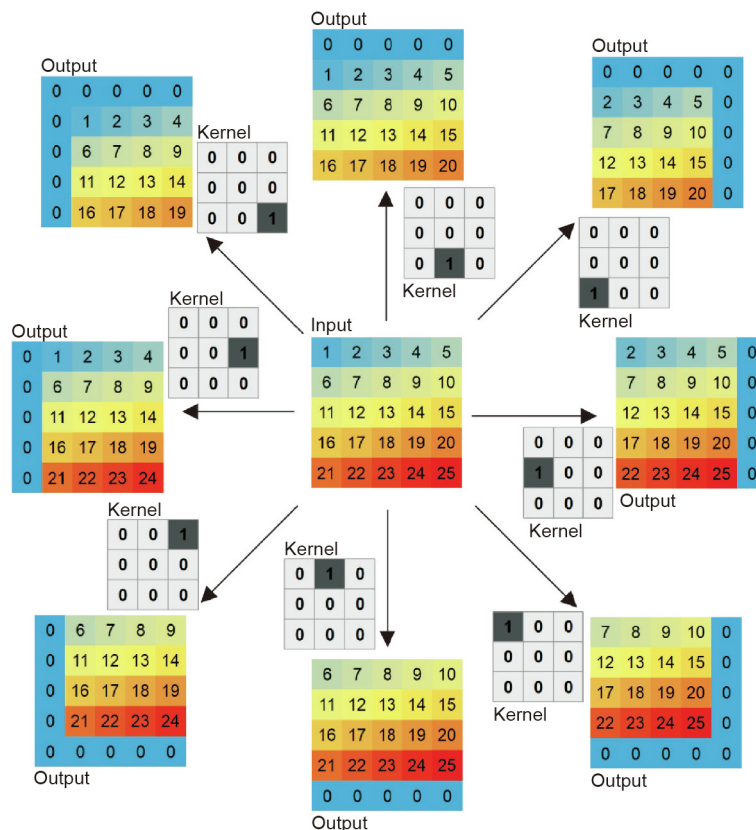


**Fig. 3.** Moving matrix with a one cell distance for eight directions with convolution.
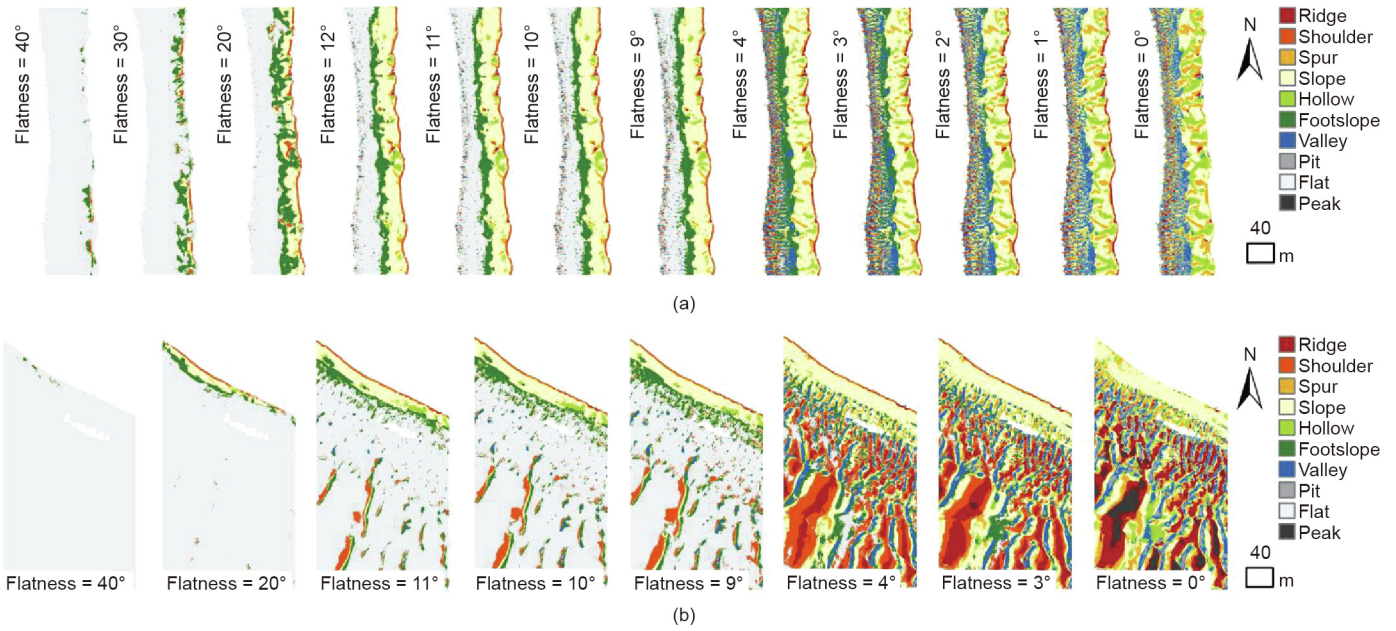
**Fig. 4.** Morphological element maps in (a) NBZ 4 and (b) NBZ 6 using geomorphons for the decrement in flatness from left to right.
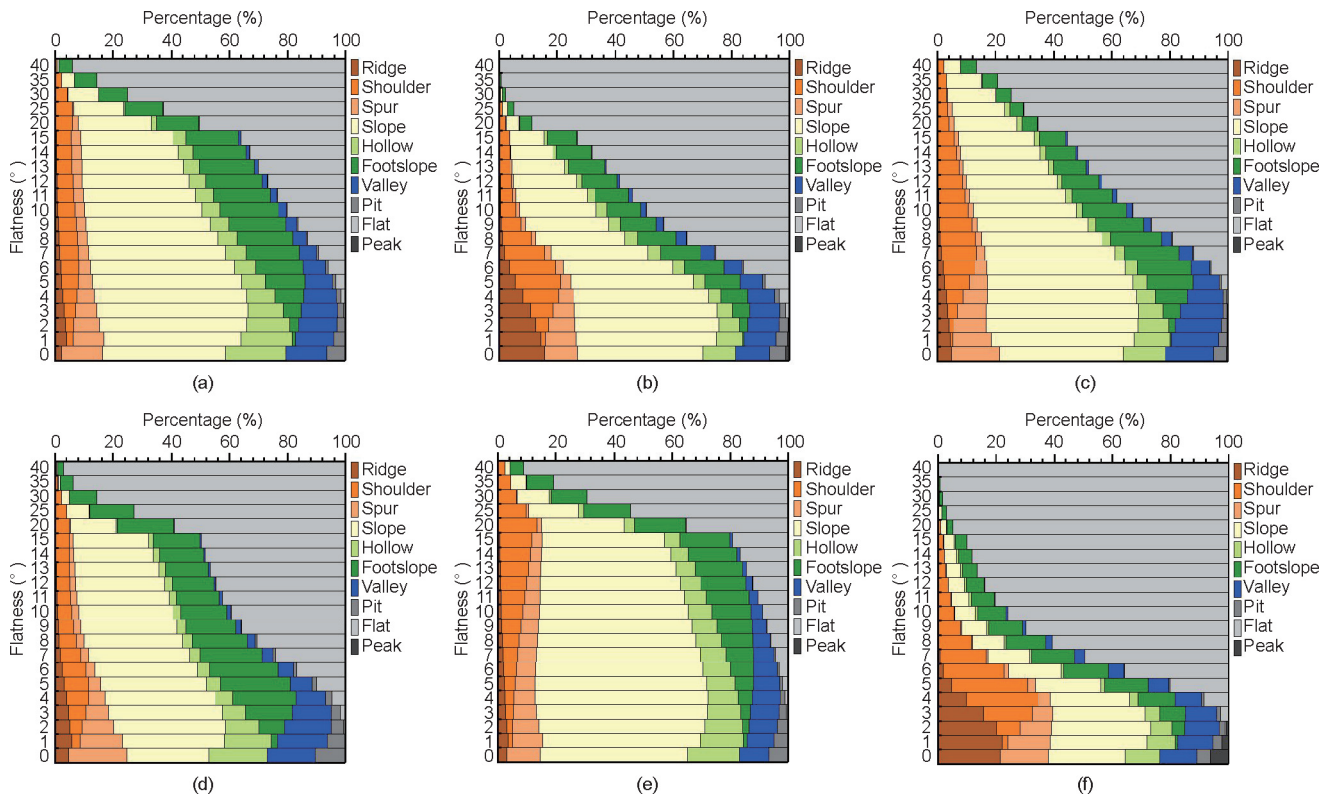


**Fig. 5.** Area statistics of the morphological elements using geomorphons for the decrement in flatness in (a–f) NBZs 1–6.

### 4.2. Morphological elements indicating bank erosion

In this study, bank scarp, scour pits, and bank scars were used as the fluvial subaqueous features to estimate bank erosion. With the decrement in flatness, an underwater surface with a high slope angle was identified as a slope cell. When the slope ratio of the slope element is relatively large, the slope cells can indicate the potential of the bank scarp to collapse (Fig. 6(a)).

The development of the scour pits can alter the shape of the bank scarp and accelerate bank erosion. Pit cells accumulating near the bank correspond to scour pits deeper than the surrounding. Bank scars result from the occurrence of collapse, indicated by hollow cells. Correspondingly, spur cells indicate the lateral boundary of the collapse (Fig. 6(b)).

Fig. 6(a) shows the bank toe in this study that can be represented by footslope cells distributed at the bottom of the bank slope. The bank toe is used to separate the bank scarp from the riverbed indicated by flat cells. Subaqueous dunes represent rhythmic terrain with alternating ridges and valleys of a wave, which is similar to the crest and trough of dunes (Fig. 6(b)).

**Table 1**
Statistical results for the ten morphological elements based on the geomorphons method.

| NBZ | Flatness (°) | Ridge | | Shoulder | | Spur | | Slope | | Hollow | |
|---|---|---|---|---|---|---|---|---|---|---|---|
| | | Number | Percentage (%) | Number | Percentage (%) | Number | Percentage (%) | Number | Percentage (%) | Number | Percentage (%) |
| 1 | 10 | 1 042 | 0.93 | 6 697 | 5.97 | 3 545 | 3.16 | 45 557 | 40.58 | 6 835 | 6.09 |
| | 0 | 2 459 | 2.19 | 0 | 0 | 15 762 | 14.04 | 47 662 | 42.46 | 23 161 | 20.63 |
| 2 | 10 | 1 055 | 0.56 | 9 866 | 5.24 | 2 298 | 1.22 | 49 735 | 26.44 | 6 825 | 3.63 |
| | 0 | 29 296 | 15.57 | 0 | 0 | 21 628 | 11.50 | 81 271 | 43.20 | 21 007 | 11.17 |
| 3 | 10 | 1 967 | 0.56 | 35 326 | 10.01 | 5 542 | 1.57 | 125 431 | 35.56 | 7 810 | 2.21 |
| | 0 | 17 140 | 4.86 | 0 | 0 | 58 235 | 16.51 | 150 055 | 42.54 | 50 857 | 14.42 |
| 4 | 10 | 921 | 0.82 | 5 547 | 4.96 | 2 569 | 2.30 | 36 259 | 32.44 | 3 096 | 2.77 |
| | 0 | 5 379 | 4.81 | 0 | 0 | 22 229 | 19.89 | 31 443 | 28.13 | 22 581 | 20.20 |
| 5 | 10 | 1 751 | 1.22 | 10 629 | 7.38 | 8 283 | 5.75 | 73 729 | 51.22 | 11 539 | 8.02 |
| | 0 | 4 442 | 3.09 | 0 | 0 | 16 554 | 11.50 | 73 138 | 50.81 | 25 312 | 17.58 |
| 6 | 10 | 234 | 0.10 | 13 537 | 5.55 | 677 | 0.28 | 16 802 | 6.88 | 2 053 | 0.84 |
| | 0 | 52 495 | 21.51 | 0 | 0 | 39 795 | 16.31 | 64 864 | 26.58 | 28 781 | 11.79 |

| NBZ | Flatness (°) | Footslope | | Valley | | Pit | | Flat | | Peak | |
|---|---|---|---|---|---|---|---|---|---|---|---|
| | | Number | Percentage (%) | Number | Percentage (%) | Number | Percentage (%) | Number | Percentage (%) | Number | Percentage (%) |
| 1 | 10 | 22 525 | 20.07 | 3 182 | 2.83 | 315 | 0.28 | 22 536 | 20.08 | 21 | 0.02 |
| | 0 | 0 | 0 | 15 994 | 14.25 | 6 953 | 6.19 | 0 | 0 | 264 | 0.24 |
| 2 | 10 | 22 225 | 11.81 | 3 184 | 1.69 | 186 | 0.10 | 92 702 | 49.28 | 37 | 0.02 |
| | 0 | 0 | 0 | 22 055 | 11.72 | 10 400 | 5.53 | 0 | 0 | 2 456 | 1.31 |
| 3 | 10 | 53 444 | 15.15 | 6 664 | 1.89 | 674 | 0.19 | 115 733 | 32.81 | 156 | 0.04 |
| | 0 | 0 | 0 | 58 952 | 16.71 | 15 022 | 4.26 | 0 | 0 | 2 486 | 0.70 |
| 4 | 10 | 17 628 | 15.77 | 1 458 | 1.30 | 284 | 0.25 | 44 025 | 39.38 | 0 | 0 |
| | 0 | 0 | 0 | 18 453 | 16.51 | 11 551 | 10.33 | 0 | 0 | 151 | 0.14 |
| 5 | 10 | 19 569 | 13.59 | 5 469 | 3.80 | 115 | 0.08 | 12 869 | 8.94 | 2 | 0 |
| | 0 | 0 | 0 | 14 797 | 10.28 | 9 436 | 6.55 | 0 | 0 | 276 | 0.19 |
| 6 | 10 | 23 619 | 9.68 | 1 577 | 0.65 | 18 | 0.01 | 185 525 | 76.02 | 3 | 0 |
| | 0 | 0 | 0 | 31 482 | 12.90 | 11 128 | 4.56 | 0 | 0 | 15 500 | 6.35 |
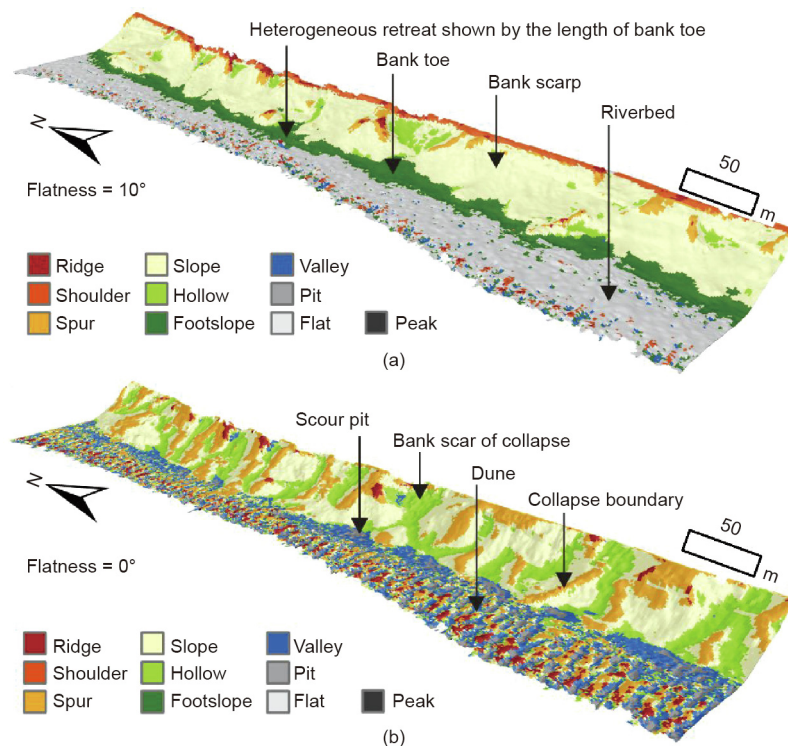


**Fig. 6.** Relationship between morphological elements and distributions of (a) the bank scarp and bank toe on the lateral profile when the flatness is 10° and (b) the bank scars from the collapse and scour pits when the flatness is 0°.

### 4.3. Key flatness for bank erosion

Fig. 7 shows morphological elements map for two key flatness. The footslope cell represents the transition from the bank scarp to riverbed. A high percentage of footslope results in a clear border between the bank scarp and riverbed. The key flatness to highlight the boundary between the bank scarp and riverbed is 10° for the relatively large occupation of footslope cells. Meanwhile, the bank scarp is covered by slope cells (Fig. 7(a)), with the location of the six profiles, indicated as bank profiles, bp01–bp06.

Fig. 8 shows six profiles drawn from the cross-section of the morphology, indicating that $L$ = 100 m is sufficient to restrict the

bank slope. The figure also demonstrates a terrain break between the bank scarp and riverbed such that the slope ratio (i.e., the ratio of slope height to length) of the profile curve covered by the slope element is between 1/3 and 1/2 and that of the curve of the foot-slope and flat is < 1/5.

Duan et al. [36] found that the stable slope ratio of a bank composed of light loam or clay soil is < 1/3 in the middle and lower reaches of the Yangtze River. Tang et al. [43] considered a stable slope ratio as a criterion to determine bank collapse. The stable slope ratio of a bank varies for different river types and geological conditions, but the stable slope range is typically approximately 1/3 to 1/2. For example, medium and fine sands have the smallest stable slope ratio range of 0.24–0.36, whereas clay has the largest stable slope ratio of 0.40–0.45. As indicated by a previous study [44], when the bank slope exceeds the stable slope ratio, it may collapse.

For the given flatness of 10°, the bank scarp with a ratio ranging from 1/3 to 1/2, which is similar to the threshold stable ratio in the
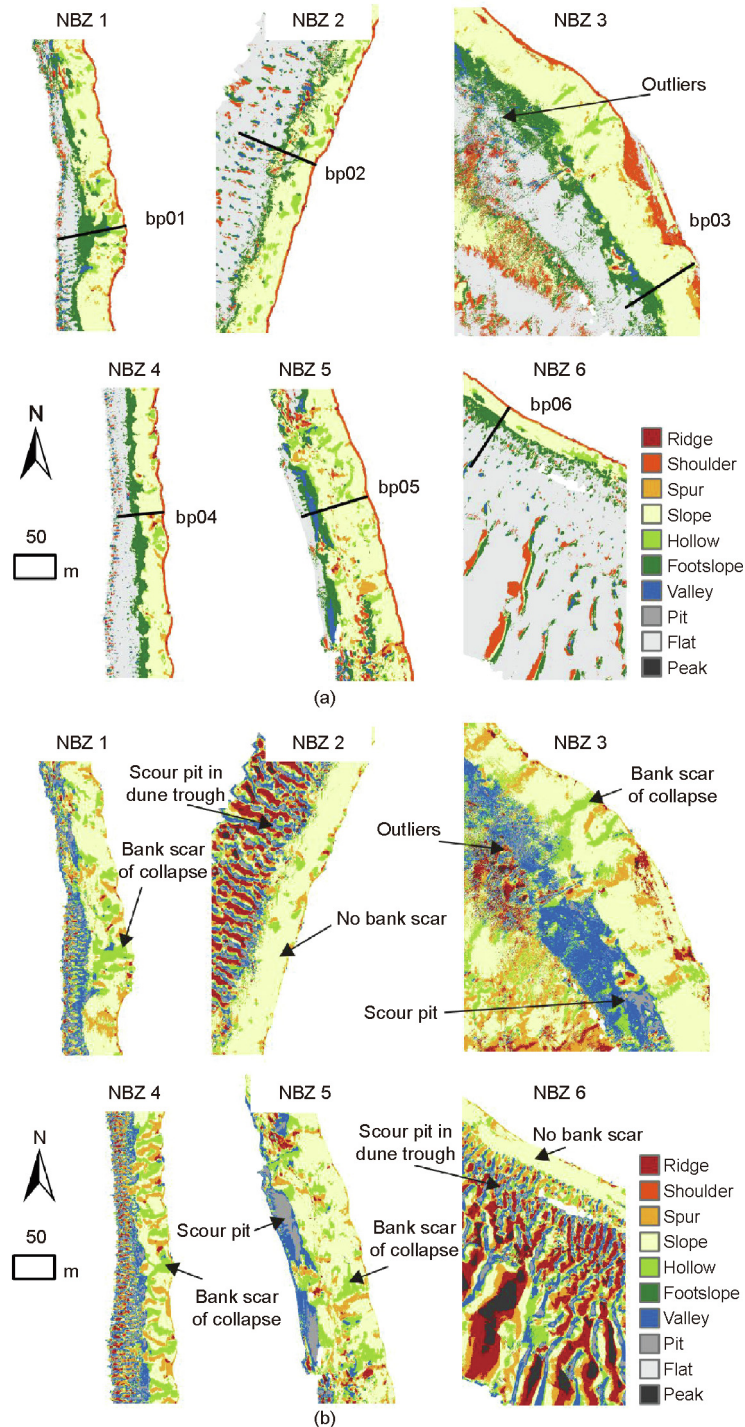


**Fig. 7.** Geomorphons-based classification results for the morphological elements in NBZs 1–6 with the location of bank profiles indicated as bp01–bp06 for a flatness of (a) 10° and (b) 0°.
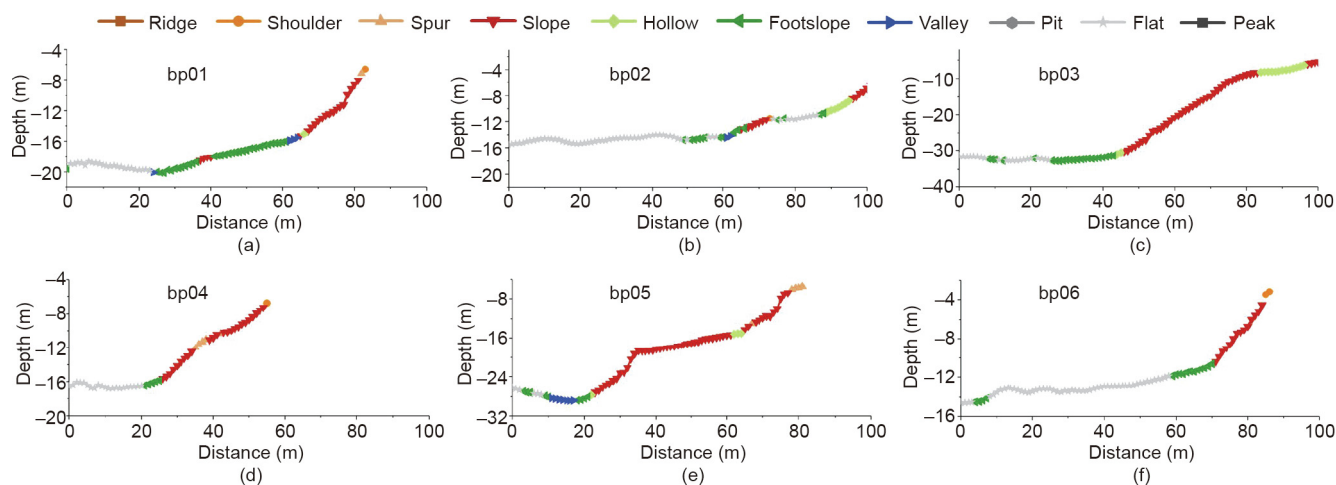
**Fig. 8.** Bank profiles from bp01–bp06 in (a)–(f), respectively, overlaid with the morphological elements.

Yangtze River, indicates that the area has the potential to collapse. The flatness should also be assigned as 10° for the bank toe and riverbed, which is equal to that of the bank scarp.

Fig. 7(b) shows that bank scars and scour pits are indicators of bank erosion, represented by hollow cells and pit cells, respectively. With the flatness of 0°, the occupation of the hollow and pit cells remained small, not exceeding 1/5 (Table 1). Fig. 4 shows that a greater flatness can lead to fewer hollow and pit cells. Therefore, 0° is considered as a key value to extract the bank erosion features of the bank scars and scour pits, as corresponding elements cover the largest area.

Dunes should be viewed as a combination of valley and ridge cells. The critical flatness for dunes should be 3°, because the ridge and valley cells are distributed in the center of the crest and trough of dunes, and the peak and pit cells have not notably expanded with the relatively low occupation. With a flatness was 0°, the dune can be indicated by a combination of ridge and peak cells and the valley and pit cells (Fig. 4), because the peak and pit cells expand from the center of the ridge and valley areas. With a flatness of $\leq 3°$, the cell number fluctuates slightly for the valley and ridge cells, forming an appropriate pattern indicating dunes. Therefore, a flatness of $\leq 3°$ is suitable for the recognition of dunes when using the geomorphons method to extract dunes in the middle reach of the Yangtze River.

Table 2 summarizes the corresponding relationships between the subaqueous morphological elements and bank erosion features for key flatness values. With a flatness of 10°, the bank scarp and riverbed are represented by the slope and flat cells, respectively. Between the bank scarp and riverbed, the footslope cells indicate the bank toe. With a flatness of 0°, the scars and boundary of the bank collapse are represented by hollow and spur cells at the bank slope, respectively. Scour pits are represented by pit cells in the depression near the bank slope. The strategy is developed for the NBZ on the side of the main channel, where a depression forms along the thalweg.

## 5. Discussion

### 5.1. Relationship between bank erosion distribution and river regime

The morphological elements in the maps presented in Fig. 7 show the distribution of the features of bank erosion. The thalweg is close to the bank at NBZs 3 and 5 (Fig. 1(b)), causing severe scour. Comparing Figs. 7(a) and (b), scour pits are located at the bank toe. The bank scarp is approximately 80 m long in NBZs 3

and 5, where the scour pits are significant with a width > 20 m. When the thalweg is away from the bank, the scour pits are not developed at the bank toe, and the bank scarp is relatively short, as in NBZs 2 and 6, with a length < 30 m. The presence of the scour pit is not notable for NBZs 1, 2, 4, and 6, where the water depth along the thalweg is < 10 m. However, the scour pit is significant for NBZs 3 and 5, which have a water depth > 11 m, indicating that a large scour pit is likely to develop at this water depth. Meanwhile, for a water depth < 10 m, smaller scour pits are distributed within the troughs of dunes, as reported by previous studies [45–47]. A subaqueous sand dune reflects an unstable bed form [48–50]. Most areas of the riverbed are active because they are covered by dunes.

The bottom of the strip collapse is near the water surface; therefore, bank scars of the strip collapse are above the water surface, as observed in the field. In contrast, the bottom of the arc collapse is under water. Therefore, bank scars are considered morphological indicators of arc collapse. Fig. 7(b) shows that the bank scars are significant in NBZs 1, 3, 4, and 5, but are absent in NBZs 2 and 6. At the location of the bank collapse, the length of the bank scarp is reduced. This indicates that the arc collapse of the bank tends to shorten the bank scarp and improves the stability of the bank slope or reduces the size of its potential collapse.

Although an editing tool was used to remove outliers, there remained many residual outliers that interrupted morphological element mapping. The riverbed was covered by flat cells, with outliers in the form of scattered points (Fig. 7(a)). Fig. 7(b) shows the outliers resulted in an unclear contour between various elements. The impact of outliers on geomorphological interpretation must be reduced in future studies.

### 5.2. Bank erosion inventory mapping

Table 2 presents the strategy that was used to guide the inventory mapping of the bank erosion in ArcGIS version 10.3. Bank erosion inventory maps were generated with zonal statistics based on near-bank units. The NBZ was divided into 169 units with an interval of 100 m. Furthermore, the bank units were overlaid with morphological element maps with flatness values of 10° and 0° to calculate the area of the bank scarp, bank scar, and scour pit using the following steps. First, the toe line of the bank slope was manually drawn based on the distribution of the dunes and bank toe. Two areas near the bank were determined based on the toe line: One was 50 m to the toe line, represented as polygon A for subsequent extraction of the scour pit, and the other is the bank slope

**Table 2**
Interpretation strategy for the bank erosion features from the morphological elements.

| Flatness | Riverbed | | Bank slope | |
|---|---|---|---|---|
| | Dunes | Depression | Gentle slope | Steep slope |
| 10° | Flat → bed | — | Footslope → bank toe | Slope → bank scarp |
| 3° | Ridge → crest of dune | — | | |
| | Valley → trough of dune | | | |
| 0° | Ridge and peak → crest of dune | Pit → scour pit | Hollow → bank scar of collapse | |
| | Valley and pit → trough of dune | | Spur → collapse boundary | |

The strategy for the near-bank zone on the side of the main channel where depression forms along the thalweg.

side within 200 m to the toe line, represented as polygon B for the bank scarp and scar. Second, the morphological element map was used to extract object cells using the "Raster Calculation" tool. Taking the bank scar as an example, the hollow was extracted from an element map with a flatness of 0°. Then, the object cells were selected as the elements for bank erosion when they are located at a suitable position near the bank using the "Extract by Mask" tool. For example, hollow cells cluster to form bank scars, but only those within polygon B were preserved. Finally, an overlay of the selected object cells in the NBZ was utilized to calculate the area of the selected object cells per unit with the "Zonal Statistics as Table" tool.

Considering these facets of mapping, the riverbank from Linjiaolao to Chenglingji has a higher risk of failure than that upstream of Linjiaolao. Fig. 9 shows that a longer bank scarp pertains to the relatively large area of scour pits based on their spatial distribution from Qizhou to Chenglingji, where the bathymetric data is relatively intact to overlap the main channel and cover the scour pit near the bank toe. Bank scars account for a larger area (i.e., area > 400 m²) when the length of the bank scarp exceeds 20 m (i.e., area > 2000 m²), indicating that bank arc collapse is prone to occur along the bank with a longer scarp.

### 5.3. Comparison of flatness for various morphologies

Flatness values vary among geomorphons-based landform and morphological delineation studies. In particular, a flatness value of 1° has been widely used for medium-resolution (10–100 m) studies in mountainous areas with an elevation difference of approximately 1000 m [26,31,33]. Moreover, the same flatness

value has been used for such studies in tributary catchments with an elevation difference of approximately 100 m [35]. Kramm et al. [32] used a flatness value of 3° and compared various grid sizes, including 5, 10, and 30 m, for landform element classification on the Loess Plateau. Most recently, Cui et al. [27] found that a flatness value of 3° was suitable for landform element detection on the seafloor with a grid size of 250 m (Table S1 in Appendix A).

This study found that a flatness larger than 40° is not useful for subaqueous morphological element mapping in the Yangtze River, because flat cells occupy approximately 95% of the area. Critical values for the flatness to map elements of the river's subaqueous bank erosion were 10° and 0°. With a flatness of 10°, the subaqueous bank scarp, bank toe, and riverbed were covered by the slope, footslope, and flat cells. With a flatness of 0°, the bank scars and scour pits were revealed by hollow and pit cells. With a flatness of 3°, the dunes were present as a combination of valley and ridge cells. Various flatness values are necessary for determining fluvial subaqueous morphological elements, in contrast to existing geomorphons-based landform and morphological delineation studies that use a specific flatness for a region. This is because the fluvial elements are mutually superimposed. For example, dunes are distributed within the riverbed, bank scars are distributed on the bank slope, and scour pits are distributed at the bank toe. A relatively large flatness can filter a relatively small roughness or texture present with a relatively small flatness. For a bank scarp with a slope ratio of approximately 1/3 to 1/2, a large flatness is necessary to separate the bank scarp from the riverbed. To extract the bank scar, scour pit, and dunes from the surface roughness and texture, a small flatness is required. Conversely, most existing studies have not considered the relationship of the
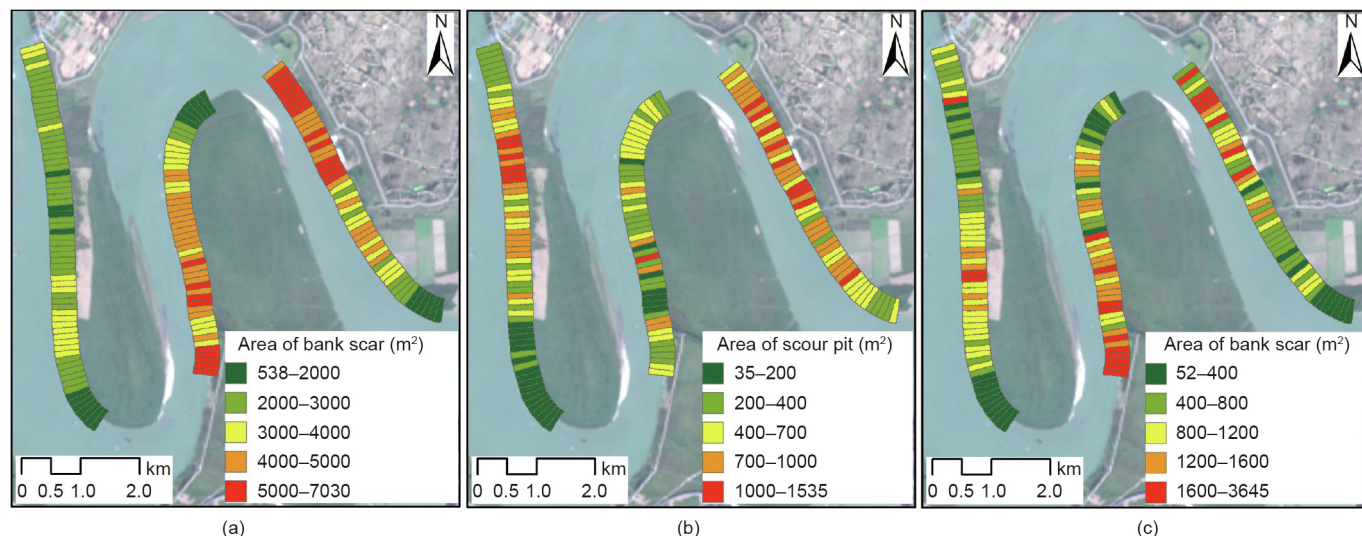


**Fig. 9.** Inventory of the bank erosion attributes drawn from the fluvial subaqueous morphological element maps, including the area of the (a) bank scarp, (b) scour pit, and (c) bank scar of the collapse.

superimposition of landform or morphological elements for terrestrial or marine environments.

## 6. Conclusions

Conventional maps generated from multibeam measurement records cannot reflect subaqueous morphological elements of bank erosion. Therefore, this study introduced a geomorphons algorithm to auto-classify subaqueous surfaces into slope, footslope, flat, ridge, peak, valley, pit, spur, hollow, and shoulder cells and examined their function as indicators of bank erosion.

In the geomorphons method, three parameters, namely the lookup distance, skip radius, and flatness, must be preset. The lookup distance controls the size of the traversal window, and a value of 100 m is sufficiently large to restrict the bank slope, scour pit, and bank scar. The skip radius was set to 3 m to eliminate outlier effects. Flatness is critical in the geomorphons-based extraction of elements. The footslope element, which is considered as a bank toe, efficiently separates the bank scarp from the riverbed with a flatness of 10°. The slope element indicates that the bank scarp is prone to collapse, because its profile curve has a slope ratio between 1/3 and 1/2, which is similar to the stable slope ratio in the middle of the Yangtze River. Hollow and pit cells better represent the areal bank scar and scour pit with the highest percentage at a flatness of 0°. At a suitable flatness, the distribution of subaqueous morphological elements is analyzed and used to map the bank erosion inventory. The analysis reveals that, on the main channel side, the NBZ with a relatively large water depth is prone to form a long bank scarp where arc collapse tends to occur. Large scour pits develop when the water depth is > 11 m and the bank scarp is stretched. Arc collapse shortens the length of the bank scarp and improves bank stability.

Flatness is also important to extract the dunes in a fluvial environment; for the Yangtze River, the efficient range of flatness for such extraction is between 0° and 3°. Various flatness values are necessary for the recognition of fluvial subaqueous morphological elements exhibiting mutual superimposition. This is different from the classification of terrestrial landform and sea floor elements achieved with one flatness value used in existing studies.

## Compliance with ethical guidelines

Ge Yan, Heqin Cheng, Zeyu Jiang, Ming Tang, Lizhi Teng, Tian Shi, Yuehua Jiang, Guoqiang Yang, and Quanping Zhou declare that they have no conflicts of interest or financial conflicts to disclose.

## Appendix A. Supplementary data

Supplementary data to this article can be found online at https://doi.org/10.1016/j.eng.2021.03.027.

## References

[1] Sekely AC, Mulla DJ, Bauer DW. Streambank slumping and its contribution to the phosphorus and suspended sediment loads of the Blue Earth River, Minnesota. J Soil Water Conserv 2002;57(5):243–50.

[2] Evans DJ, Gibson CE, Rossell RS. Sediment loads and sources in heavily modified Irish catchments: a move towards informed management strategies. Geomorphology 2006;79(1–2):93–113.

[3] Wilson CG, Kuhnle RA, Bosch DD, Steiner JL, Starks PJ, Tomer MD, et al. Quantifying relative contributions from sediment sources in Conservation Effects Assessment Project watersheds. J Soil Water Conserv 2008;63(6):523–32.

[4] Henshaw AJ, Thorne CR, Clifford NJ. Identifying causes and controls of river bank erosion in a British upland catchment. Catena 2013;100:107–19.

[5] Marteau B, Vericat D, Gibbins C, Batalla RJ, Green DR. Application of structure-from-motion photogrammetry to river restoration. Earth Surf Process Landf 2017;42(3):503–15.

[6] Xia J, Zong Q, Deng S, Xu Q, Lu J. Seasonal variations in composite riverbank stability in the Lower Jingjiang Reach, China. J Hydrol 2014;519:3664–73.

[7] Konsoer KM, Rhoads BL, Langendoen EJ, Best JL, Ursic ME, Abad JD, et al. Spatial variability in bank resistance to erosion on a large meandering, mixed bedrock-alluvial river. Geomorphology 2016;252:80–97.

[8] Gilvear DJ, Davies JR, Winterbottom SJ. Mechanisms of floodbank failure during large flood events on the rivers Tay and Earn, Scotland. Q J Eng Geol Hydrogeol 1994;27(4):319–32.

[9] Kummu M, Lu XX, Rasphone A, Sarkkula J, Koponen J. Riverbank changes along the Mekon River: remote sensing detection in the Vientiane–Nong Khai area. Quat Int 2008;186(1):100–12.

[10] Sarkar A, Garg RD, Sharma N. RS-GIS based assessment of river dynamics of Brahmaputra River in India. J Water Resource Prot 2012;04(02):63–72.

[11] Winterbottom SJ, Gilvear DJ. A GIS-based approach to mapping probabilities of river bank erosion: regulated River Tummel, Scotland. Regul Rivers Res Manage 2000;16(2):127–40.

[12] Bandyopadhyay S, Ghosh K, De SK. A proposed method of bank erosion vulnerability zonation and its application on the River Haora, Tripura, India. Geomorphology 2014;224:111–21.

[13] Midgley TL, Fox GA, Heeren DM. Evaluation of the bank stability and toe erosion model (BSTEM) for predicting lateral retreat on composite streambanks. Geomorphology 2012;145–146:107–14.

[14] Deng S, Xia J, Zhou M, Lin F. Coupled modeling of bed deformation and bank erosion in the Jingjiang Reach of the middle Yangtze River. J Hydrol 2019;568:221–33.

[15] Hackney C, Best J, Leyland J, Darby SE, Parsons D, Aalto R, et al. Modulation of outer bank erosion by slump blocks: disentangling the protective and destructive role of failed material on the three-dimensional flow structure. Geophys Res Lett 2015;42(24):10663–70.

[16] Jugie M, Gob F, Virmoux C, Brunstein D, Tamisier V, Le Coeur C, et al. Characterizing and quantifying the discontinuous bank erosion of a small low energy river using structure-from-motion Photogrammetry and erosion pins. J Hydrol 2018;563:418–34.

[17] Twichell DC, Chaytor JD, ten Brink US, Buczkowski B. Morphology of late Quaternary submarine landslides along the US Atlantic continental margin. Mar Geol 2009;264(1–2):4–15.

[18] Puga-Bernabéu Á, Webster JM, Beaman RJ, Guilbaud V. Morphology and controls on the evolution of a mixed carbonate–siliciclastic submarine canyon system, Great Barrier Reef margin, north-eastern Australia. Mar Geol 2011;289(1–4):100–16.

[19] McAdoo BG, Pratson LF, Orange DL. Submarine landslide geomorphology, US continental slope. Mar Geol 2000;169(1–2):103–36.

[20] Green A, Uken R. Submarine landsliding and canyon evolution on the northern KwaZulu-Natal continental shelf, South Africa, SW Indian Ocean. Mar Geol 2008;254(3–4):152–70.

[21] Wood J. The geomorphological characterisation of digital elevation models [dissertation]. Leicester: University of Leicester; 1996.

[22] MacMillan RA, Pettapiece WW, Nolan SC, Goddard TW. A generic procedure for automatically segmenting landforms into landform elements using DEMs, heuristic rules and fuzzy logic. Fuzzy Sets Syst 2000;113(1):81–109.

[23] Adediran AO, Parcharidis I, Poscolieri M, Pavlopoulos K. Computer-assisted discrimination of morphological units on north–central Crete (Greece) by applying multivariate statistics to local relief gradients. Geomorphology 2004;58(1–4):357–70.

[24] Schmidt J, Hewitt A. Fuzzy land element classification from DTMs based on geometry and terrain position. Geoderma 2004;121(3–4):243–56.

[25] Drăguţ L, Blaschke T. Automated classification of landform elements using object-based image analysis. Geomorphology 2006;81(3–4):330–44.

[26] Jasiewicz J, Stepinski TF. Geomorphons—a pattern recognition approach to classification and mapping of landforms. Geomorphology 2013;182:147–56.

[27] Cui X, Xing Z, Yang F, Fan M, Ma Y, Sun Yi. A method for multibeam seafloor terrain classification based on self-adaptive geographic classification unit. Appl Acoust 2020;157:107029.

[28] Di Stefano M, Mayer LA. An automatic procedure for the quantitative characterization of submarine bedforms. Geosciences 2018;8(1):28.

[29] Debese N, Jacq JJ, Garlan T. Extraction of sandy bedforms features through geodesic morphometry. Geomorphology 2016;268:82–97.

[30] Libohova Z, Winzeler HE, Lee B, Schoeneberger PJ, Datta J, Owens PR. Geomorphons: landform and property predictions in a glacial moraine in Indiana landscapes. Catena 2016;142:66–76.

[31] Campos Pinto L, de Mello CR, Norton LD, Owens PR, Curi N. Spatial prediction of soil–water transmissivity based on fuzzy logic in a Brazilian headwater watershed. Catena 2016;143:26–34.

[32] Kramm T, Hoffmeister D, Curdt C, Maleki S, Khormali F, Kehl M. Accuracy assessment of landform classification approaches on different spatial scales for the Iranian loess plateau. ISPRS Int J Geoinf 2017;6(11):366.

[33] Luo W, Liu CC. Innovative landslide susceptibility mapping supported by geomorphon and geographical detector methods. Landslides 2018;15(3): 465–74.

[34] Chea H, Sharma M. Residential segregation in hillside areas of Seoul, South Korea: a novel approach of geomorphons classification. Appl Geogr 2019;108:9–21.

[35] Flynn T, Rozanov A, de Clercq W, Warr B, Clarke C. Semi-automatic disaggregation of a national resource inventory into a farm-scale soil depth class map. Geoderma 2019;337:1136–45.

[36] Duan J, Duan W, Zhu J. Analysis of riverbank sloughing and stability. Eng J Wuhan Univ 2004;37(6):17–21. Chinese.

[37] Zhang X, Jiang C, Chen Q, Ying Q. Types and features of riverbank collapse. Adv Sci Technol Water Resour 2008;28(5):66–70.

[38] Xu Y, Liang Z, Wang X, Li W, Du Y. Analysis on bank failure and river channel changes. J Sediment Res 2001;4:41–6.

[39] Jin L, Wang N, Fu Q. Analysis of topography of bank-slides and its affecting factors in Mahu reach of the Yangtze River. J Sediment Res 1998;2:67–71.

[40] Peng Y, Xiong C, Yang C. Analysis of relationship between fluvial process and bank caving in the Jingjiang Reach of Yangtze River. J China Hydrol 2010;30(6): 29–36.

[41] Liao WH. Region description using extended local ternary patterns. In: Proceedings of the 20th International Conference on Pattern Recognition; 2010 Aug 23–26; Istanbul, Turkey. New York City: IEEE; 2010.

[42] Yokoyama R, Shirasawa M, Pike RJ. Visualizing topography by openness: a new application of image processing to digital elevation models. Photogramm Eng Remote Sensing 2002;68(3):257–66.

[43] Tang J, Deng J, You X, Wang F. Forecast method for bank collapse in middle and lower Yangtze River. J Sichuan Univ 2012;44(1):75–81.

[44] Wang YG, Kuang SF. Study on types and collapse modes of bank failures. J Sediment Res 2014;1:13–20.

[45] Zheng S, Cheng H, Wu S, Liu G, Lu X, Xu W. Discovery and implications of catenary-bead subaqueous dunes. Sci China Earth Sci 2016;59(3):495–502.

[46] Zheng S, Cheng H, Wu S, Shi S, Xu W, Zhou Q, et al. Morphology and mechanism of the very large dunes in the tidal reach of the Yangtze River. China. Cont Shelf Res 2017;139:54–61.

[47] Zheng S, Cheng H, Shi S, Xu W, Zhou Q, Jiang Y, et al. Impact of anthropogenic drivers on subaqueous topographical change in the Datong to Xuliujing Reach of the Yangtze River. Sci China Earth Sci 2018;61(7):940–50.

[48] Cheng HQ, Kostaschuk R, Shi Z. Tidal currents, bed sediments, and bedforms at the South Branch and the South Channel of the Changjiang (Yangtze) estuary, China: implications for the ripple-dune transition. Estuaries 2004;27(5): 861–6.

[49] Cheng H, Li J, Yin D, Li M, Wang B. Nearshore bedform instability in the eastern entrance to the Qiongzhou Strait, South China Sea. Front Earth Sci China 2008;2(3):283–91.

[50] Cheng H, Teng L, Chen W. Dune dynamics in coarse silt, sand and gravel along the main channel from the estuarine front of the Yangtze River to the Three Gorges Dam. In: Proceedings of the Marine and River Dune Dynamics; 2019 Apr 1–2; Bremen, Germany; 2019.